

1 **Estimation of oceanic sub-surface mixing under a severe cyclonic storm**
2 **using a coupled atmosphere-ocean-wave model**

3 Kumar Ravi Prakash, Tanuja Nigam, Vimlesh Pant

4 Centre for Atmospheric Sciences, Indian Institute of Technology Delhi, New Delhi-110016

5
6 **Abstract**

7 A coupled atmosphere-ocean-wave model used to examine mixing in the upper oceanic
8 layers under the influence of a very severe cyclonic storm Phailin over the Bay of Bengal (BoB)
9 during 10-14 October 2013. Model simulations highlight prominent role of cyclone induced near-
10 inertial oscillations in sub-surface mixing up to the thermocline depth. The inertial mixing
11 introduced by the cyclone played a central role in deepening of the thermocline and mixed layer
12 depth by 40 m and 15 m, respectively. For the first time over the BoB, a detailed analysis of inertial
13 oscillation kinetic energy generation, propagation, and dissipation was carried out using an
14 atmosphere-ocean-wave coupled model during a cyclone. A quantitative estimate of kinetic energy
15 in the oceanic water column, its propagation and dissipation mechanisms were explained using the
16 coupled atmosphere-ocean-wave model. The large shear generated by the inertial oscillations
17 found to overcome the stratification and initiate mixing at the base of the mixed layer. Greater
18 mixing was found at the depths where the eddy kinetic diffusivity was large. The baroclinic
19 current, holding a larger fraction of kinetic energy than the barotropic current, weakened rapidly
20 after the passage of cyclone. The shear-induced by inertial oscillations found to decrease rapidly
21 with increasing depth below the thermocline. The dampening of mixing process below the
22 thermocline explained through the enhanced dissipation rate of turbulent kinetic energy upon
23 approaching the thermocline layer. The wave-current interaction, non-linear wave-wave
24 interaction were found to affect the process of downward mixing and cause the dissipation of
25 inertial oscillations.

26
27 **1. Introduction**

28 The Bay of Bengal (BoB), a semi-enclosed basin in the northeastern Indian ocean, consists
29 of surplus near-surface fresh water due to large precipitation and runoff from the major river

30 systems of the Indian subcontinent (Varkey et al., 1996; Rao and Sivakumar, 2003; Pant et al.,
31 2015). Presence of fresh water leads to salt-stratified upper ocean water column and formation of
32 barrier layer (BL), a layer sandwiched between bottom of the mixed layer (ML) and top of the
33 thermocline, in the BoB (Lukas and Lindstrom, 1991; Vinayachandran et al., 2002; Thadathil et
34 al., 2007). The BL restricts entrainment of colder waters from thermocline region into the mixed
35 layer thereby, maintains warmer ML and sea surface temperature (SST). The warmer SST together
36 with higher tropical cyclone heat potential (TCHP) makes the BoB as one of the active regions for
37 cyclogenesis (Suzana et al. 2007; Yanase et al. 2012, Vissa et al. 2013). Majority of tropical
38 cyclones generate during the pre-monsoon (April-May) and post-monsoon (October-November)
39 seasons (Alam et al., 2003; Longshore, 2008). The number of cyclones and their intensity is highly
40 variable in seasonal and interannual time scales. The oceanic response to the tropical cyclone
41 depends on the stratification of the ocean. The BL formation in the BoB is associated with the
42 strong stratification due to the peak discharge from rivers in the post-monsoon season. The
43 intensity of the cyclone largely depends on the degree of stratification (Neetu et al. 2012; Li et al.
44 2013). The coupled atmosphere-ocean model found to improve the intensity of cyclonic storm
45 when compared to the uncoupled model over different oceanic regions (Warner et al., 2010;
46 Zambon et al., 2014; Srinivas et al., 2016; Wu et al., 2016). Zambon et al. (2014) compared the
47 simulations from the coupled atmosphere-ocean and uncoupled models and reported significant
48 improvement in the intensity of storm in the coupled case as compared to the uncoupled case. The
49 uncoupled atmospheric model produced large ocean-atmosphere enthalpy fluxes and stronger
50 winds in the cyclone (Srinivas et al., 2016). When the atmospheric model WRF was allowed
51 interactions with the ocean model, the SST found to be more realistic as compared to warm bias
52 in the stand-alone WRF (Warner et al., 2010). Wu et al. (2016) demonstrated the advantage of
53 using a coupled model over the uncoupled model in better simulation of typhoon Megi's intensity.

54 Mixing in the water column has an important role in energy and material transference.
55 Mixing in the ocean can be introduced by the different agents such as wind, current, tide, eddy,
56 and cyclone. Mixing due to tropical cyclones is mostly limited to the upper ocean but the cyclone-
57 induced internal waves can affect the subsurface mixing. Several studies have observed that the
58 mixing in the upper oceanic layer is introduced due to the generation of near-inertial oscillations
59 (NIO) during the passage of tropical cyclones (Gonella, 1971; Shay et al., 1989; Johanston et al.,
60 2016). This mixing is responsible for deepening of ML and shoaling of the thermocline (Gill,

61 1984). The vertical mixing caused by storm-induced NIO has a significant impact on the upper
62 ocean variability (Price, 1981). The NIO are also found to be responsible for the decrement of SST
63 along the cyclone track (Chang and Anthes, 1979; Leipper, 1967; Shay et al., 1992; Shay et al.,
64 2000). This decrease in SST is caused by the entrainment of cool subsurface thermocline water in
65 the mixed layer into the immediate overlying layer of water. This cooling of surface water is one
66 of the reason for the decay of cyclone (Cione and Uhlhorn, 2003). The magnitude of surface
67 cooling differs largely depending on the degree of stratification at the rightward to the cyclone
68 track (Jacob, 2003; Price et al., 1981).

69 The near-inertial process can be analyzed from the baroclinic component of currents. The
70 vertical shear of horizontal baroclinic velocities that is interrelated to buoyancy oscillations of
71 surface layers is utilized in various studies to have an adequate understanding of the mixing
72 associated with high frequency oscillations i.e. NIO (Zhang et al., 2014). The shear generated due
73 to NIO is an important factor for the intrusion of the cold thermocline water into the ML during
74 near-inertial scale mixing (Price et al., 1978; Shearman, 2005; Burchard and Rippeth, 2009). The
75 alternative upwelling and downwelling features of the temperature profile are an indication of the
76 inertial mixing. The Kinetic energy bounded with these components of current shows a rise in
77 magnitude at the right side of cyclone track (Price et al., 1981; Sanford et al., 1987; Jacob, 2003).
78 The reason for this high magnitude of kinetic energy is linked with strong wind and rotating wind
79 vector condition of the storm. The spatial distribution of near-inertial energy is primarily controlled
80 by the boundary effect for inertial oscillations (Chen et al., 2017). The NIO energy found to decline
81 with the decreasing depth and vanish in the coastal regions (Schahinger, 1988; Chen et al., 2017).

82 The aim of this paper is to understand and quantify the near-inertial mixing due to the very
83 severe cyclonic storm Phailin in the BoB. Phailin was developed over the BoB in the northern
84 Indian ocean in October 2013. The landfall of Phailin occurred on 12 October 2013 around 15:30
85 GMT near Gopalpur district of Odisha state on the east coast of India. After the 1999 super
86 cyclonic event of the Odisha coast, Phailin was the second strongest cyclonic event that made
87 landfall on the east coast of India (Kumar and Nair, 2015). The low-pressure system developed in
88 the north of the Andaman Sea on 7th October 2013, which transformed into a depression on 8th
89 October at 12 °N, 96 °E. This depression got converted to a cyclonic disturbance on 9th October
90 and further intensified while moved to east-central BoB and opted the maximum wind speed of

91 200 km h⁻¹ at 03:00 GMT on 11th October. Finally, landfall occurs at 17:00 GMT 12th October.
92 More details on the development and propagation of Phailin can be found in the literature (IMD
93 Report, 2013; Mandal et al. 2015). The performance of the coupled atmosphere-ocean model in
94 simulating the oceanic parameters temperature, salinity, and currents during the Phailin is accessed
95 in Prakash and Pant (2017).

96 Most of the past studies on the oceanic mixing under cyclonic conditions were carried out
97 using in-situ measurements, which are constrained by the spatial and temporal availability. To the
98 best of our knowledge, the present study is first of its kind that utilizes a coupled atmosphere-
99 ocean-wave model over the BoB to estimate the cyclone-induced mixing and associated energy
100 propagation at the cyclone track and a location of maximum surface wind stress during the period
101 of peak intensity of the cyclone. The study also focuses on analyzing the subsurface distribution
102 of NIO with its vertical mixing potential. Further, the study quantifies the shear generated mixing
103 and the kinetic energy of the baroclinic mode of horizontal current varying in the vertical section
104 at a selected location during the active period of the cyclone. The dissipation rate of NIO and
105 turbulent eddy diffusivity are quantified.

106

107 **2. Data and Methodology**

108 **2.1 Model details**

109 Numerical simulations during the period of Phailin were carried out using the coupled
110 ocean-atmosphere-wave-sediment transport (COAWST), described in detail by Warner et al.
111 (2010). COAWST modeling system couples the three-dimensional oceanic model ‘Regional
112 Ocean Modeling System’ (ROMS), the atmospheric model ‘Weather Research and Forecasting’
113 (WRF), and the wind wave generation and propagation model ‘Simulating Waves Nearshore’
114 (SWAN). ROMS model used for the study is a free surface, primitive equation, sigma coordinate
115 model. ROMS is a hydrostatic ocean model that solves finite difference approximations of the
116 Reynolds averaged Navier-Stokes equations (Chassignet et al., 2000; Haidvogel et al., 2000,
117 Haidvogel et al., 2008; Shchepetkin and McWilliams, 2005). The atmospheric model component
118 in the COAWST is a non-hydrostatic, compressible model ‘Advanced Research Weather Research
119 Forecast Model’ (WRF-ARW), described in Skamarock et al. (2005). It has different schemes for

120 representation of boundary layer physics and physical parameterizations of sub-grid scale
121 processes. In the COAWST modeling system, appropriate modifications were made in the code of
122 atmospheric model component to provide an improved bottom roughness from the calculation of
123 the bottom stress over the ocean (Warner et al., 2010). Further, the momentum equation is modified
124 to improve the representation of surface waves. The modified equation needs the additional
125 information of wave energy dissipation, propagation direction, wave height, wavelength that are
126 obtained from wave component of the COAWST model. The spectral wave model SWAN, used in
127 the COAWST modeling system, is designed for shallow water. The wave action balance equation is
128 solved in the wave model for both spatial and spectral spaces (Booij et al. 1999). The SWAN model
129 used in the COAWST system includes the wave-wind generation, wave-breaking, wave-dissipation, and
130 nonlinear wave-current-wind interaction. The ‘Model Coupling Toolkit’ (MCT) used as a coupler in the
131 COAWST modeling system to couple different model components (Larson et al., 2004; Jacob et al., 2005).
132 The coupler utilizes a parallel-coupled approach to facilitate the transmission and transformation of various
133 distributed parameters among component models. MCT coupler exchanges prognostic variables from one
134 model to another model component as shown in Figure 1. The WRF model receives sea surface temperature
135 (SST) from the ROMS model and supplies the zonal (Uwind) and meridional (Vwind) components of 10-
136 m wind, atmospheric pressure (Patm), relative humidity (RH), cloud fraction (Cloud), precipitation (Rain),
137 shortwave (Swrad) and longwave (Lwrad) radiation to the ROMS model. The SWAN model receives
138 Uwind and Vwind from the WRF model and transfers significant wave height (Hwave) and mean
139 wavelength (Lmwave) to the WRF model. A large number of variables are exchanged between ROMS and
140 SWAN models. The ocean surface current components (U_s , V_s), free surface elevations (η), and bathymetry
141 (Bath) provided to the SWAN from ROMS model. The wave parameters i.e. Hwave, Lmwave, peak
142 wavelength (Lpwave), wave direction (Dwave), surface wave period (Tpsurf), bottom wave period
143 (Tmbott), percentage wave breaking (Qb), wave energy dissipation (DISSwcap), and bottom orbit velocity
144 (Ubot) provided from the SWAN to ROMS model through the MCT coupler. Further details on the
145 COAWST modeling system can be found in Warner et al. (2010).

146

147 **2.2 Model configuration and experiment design**

148 The coupled model was configured over the BoB to study the Phailin during the period of
149 00 GMT 10 October – 00 GMT 15 October 2013. The setup of COAWST modeling system used
150 in this study included fully coupled atmosphere-ocean-wave (ROMS+WRF+SWAN) models but

151 the sediment transport is not included. A non-hydrostatic, fully compressible atmospheric model
152 with a terrain-following vertical coordinate system, WRF-ARW (version 3.7.1) was used in the
153 COAWST configuration. The WRF model used with 9 km horizontal grid resolution over the domain 65
154 °E-105 °E, 1°N-34 °N and 30 sigma levels in the vertical. The WRF was initialized with ‘National Centre
155 for Environmental Prediction’ (NCEP) ‘Final Analysis’ (FNL) data (NCEPFNL, 2000) at 00 GMT 10
156 October 2013. The lateral boundary conditions in WRF were provided at 6 hour interval from the FNL data.
157 We used the parameterization schemes for calculating boundary layer processes, precipitation
158 processes, and surface radiation fluxes. The Monin-Obukhov scheme of surface roughness layer
159 parameterization (Monin and Obukhov 1954) was activated in the model. The Rapid Radiation
160 Transfer Model (RRTM) and cloud-interactive shortwave (SW) radiation scheme from Dudhia
161 (1989) were used. The planetary boundary layer scheme YSU-PBL, described by Noh et al. (2003),
162 was used. At each time step, the calculated value of exchange coefficients and surface fluxes off
163 the land or ocean surface by the atmospheric and land surface layer models (NOAH) passed to the
164 YSU PBL. The Grid-scale precipitation processes were represented by WRF single-moment
165 (WSM) six-class moisture microphysics scheme by Hong and Lim (2006). The sub-grid scale
166 convection and cloud detrainment were taken care by Kain (2004) cumulus scheme.

167 A terrain following ocean model ROMS with 40 sigma levels in the vertical used in this
168 study. The ROMS model domain used with zonal and meridional grid resolutions of 6 km and 4 km,
169 respectively. This high resolution in ROMS enables to resolve mesoscale eddies in the ocean. The vertical
170 stretching parameters i.e. θ_s and θ_b were set at 7 and 2, respectively. The northern lateral boundary in ROMS
171 was closed by the Indian subcontinent. The ROMS model observed open lateral boundaries in the west,
172 east, and south in the present configuration. The initial and lateral open boundary conditions were derived
173 from the ‘Estimating the Circulation and Climate of the Ocean, Phase II’ (ECCO2) data (Menemenlis et
174 al., 2005). The ocean bathymetry was provided from the 2-minute gridded global relief (ETOPO2) data
175 (National Geophysical Data Center, 2006). There was no relaxation provided to the model for any
176 correction in the temperature, salinity, and current fields. The Generic-Length-Scale (GLS) vertical
177 mixing scheme parameterized as the K- ϵ model used (Warner et al., 2005). Tidal boundary
178 conditions were derived from the TPXO.7.2 (<ftp://ftp.oce.orst.edu/dist/tides/Global>) data, which
179 includes phase and amplitude of the M2, S2, N2, K2, K1, O1, P1, MF, MM, M4, MS4, and MN4
180 tidal constituents along the east coast of India. The tidal input was interpolated from TPXO.7.2
181 grid to ROMS computational grid. The Shchepetkin boundary condition (Shchepetkin, 2005) for

182 the barotropic current was used at open lateral boundaries of the domain which allowed the free
183 propagation of astronomical tide and wind-generated currents. The domains of atmosphere and
184 ocean models are shown in Figure 2. The ROMS and SWAN were configured over the common
185 model domain shown with the shaded bathymetry data in Figure 2. The two locations used for the
186 time series analysis are marked with stars in Figure 2. These two locations, one on-track and
187 another off-track, were selected in the vicinity of the region of maximum surface cooling and wind-
188 stress during the passage of Phailin. The wave model SWAN was forced with the WRF computed wind
189 field. We used 24 frequency (0.04 - 1.0 Hz) and 36 directional bands in SWAN model. The boundary
190 conditions for SWAN were derived from the ‘WaveWatch III’ model. In the COAWST system, the free
191 surface elevations (ELV) and current (CUR) simulated by ocean model ROMS are provided to the wave
192 model SWAN. The Kirby and Chen (1998) formulation was used for the computation of currents. The
193 surface wind applied to the SWAN model (provided by WRF) used in the Komen et al. (1984) closure
194 model to transfer energy from the wind to the wave field. The baroclinic time step used in ROMS model
195 was 5 s. The SWAN and WRF models used with time steps of 120 s and 60 s, respectively. The coupled
196 modeling system allows the exchange of prognostic variables among the atmosphere, ocean, and
197 wave models at every 600 s. The SST simulation at high spatial and temporal resolutions enables
198 accurate heat fluxes at the air-sea interface and exchange of heat between oceanic mixed layer and
199 atmospheric boundary layer. The surface roughness parameter calculated in the WRF model based
200 on Taylor and Yelland (2001), which involved parameters from the wave model.

201

202 **2.3. Methodology**

203 The baroclinic current component was calculated by subtracting the barotropic component
204 from the mean current with a resolution of 2 m in the vertical. The power spectrum analysis was
205 performed on the zonal and meridional baroclinic currents along the depth section of the selected
206 locations by using periodogram method (Auger and Flandrin, 1995). The continuous wavelet
207 transform using Morlet wavelet method (Lilly and Olhede, 2012) carried out to analyze the
208 temporal variability of the baroclinic current at a particular level of 14 m. The near-inertial
209 baroclinic velocities were filtered by the Butterworth 2nd order scheme for the cutoff frequency
210 range of 0.028 to 0.038 cycle hr⁻¹. The filtered zonal (u_f) and meridional (v_f) inertial baroclinic

211 currents were used to calculate the inertial baroclinic kinetic energy (E_f) in $m^2 s^{-2}$ and inertial shear
 212 (S_f) following Zhang et al. (2014) using equation (1).

$$213 \quad S_f^2 = \left(\frac{\partial u_f}{\partial z}\right)^2 + \left(\frac{\partial v_f}{\partial z}\right)^2 \quad (1)$$

214 As the stratification is a measure of oceanic stability, the buoyancy frequency (N) was calculated
 215 using equation (2)

$$216 \quad N^2 = -\frac{g}{\rho} \frac{\partial \rho}{\partial z} \quad (2)$$

217 Where ρ is the density of seawater and g is the acceleration due to gravity.

218 The analysis of generation of the inertial oscillations and their dissipation was performed
 219 on the basis of turbulent dissipation rate (ϵ) and turbulent eddy diffusivity (k_ρ). These parameters
 220 were calculated by using following formula (Mackinnon and Gregg, 2005; van der Lee and
 221 Umlauf, 2011; Palmer et al., 2008; Osborn, 1980)

$$222 \quad \epsilon = \epsilon_0 \left(\frac{N}{N_0}\right) \left(\frac{S_{lf}}{S_0}\right) \quad (3)$$

$$223 \quad k_\rho = 0.2 x \left(\frac{\epsilon}{N^2}\right) \quad (4)$$

224 Where S_{lf} is the low shear background velocity, Values of $N_0 = S_0 = 3$ cycle per hour and $\epsilon_0 =$
 225 $10^{-8} W kg^{-1}$.

226

227 **3. Results and Discussion**

228 **3.1. Validation of coupled model simulations**

229 The WRF model simulated track of Phailin was validated against the India Meteorological
 230 Department (IMD) reported best-track of the cyclone. A comparison of model simulated track with
 231 the IMD track is shown in Figure 3. Solid circles marked on both the tracks represent the 3-hourly
 232 positions of the cyclone's center, as identified by the minimum surface pressure. The daily
 233 positions of the centre of Phailin are labelled with the date. WRF model in the coupled
 234 configuration does a fairly good job in simulating the track, translational speed, and landfall

235 location of Phailin. The positional track error was about 40 km when compared to IMD track of
236 Phailin. The stand-alone WRF model (not shown here) was found to simulate Phailin track almost
237 similar to the WRF in coupled configuration. However, the intensity (surface wind speed) in WRF
238 stand-alone model was higher as compared to the coupled model. Figure 4 shows the comparison
239 of stand-alone WRF and coupled model simulated mean sea level pressure (MSLP), wind speed,
240 and wind direction at a buoy (BD09) location (marked with a blue circle in Figure 3). It can be
241 inferred from the figure that stand-alone WRF simulated larger pressure drop and higher wind
242 speed as compared to buoy measurements. The WRF in coupled model configuration shows better
243 performance in simulating the surface wind speed and pressure during Phailin. The exchange of
244 wave parameters with the WRF model in coupled configuration provides realistic sea surface
245 roughness that resulted in improvement of surface wind speed.

246 The SST simulated by the ROMS model in coupled and stand-alone configurations was
247 validated against the Advanced Very High Resolution Radiometer (AVHRR) satellite data on each
248 day for the period of Phailin passage over the BoB. Figure 5 shows that the coupled model captures
249 the SST spatial pattern reasonably well with about -0.5°C bias in northwestern BoB on 13-14
250 October. This order of bias in SST could be resulted from the errors in initial and boundary
251 conditions provided to the model. The maximum cooling of the sea surface observed on 13th
252 October in the northwestern BoB in both, coupled model and observations. This post-cyclone
253 cooling primarily associated with the cyclone-induced upwelling resulting from the surface
254 divergence driven by the Ekman transport. Thus, the coupled model is reproducing dynamical
255 processes and vertical velocities reasonably well. The stand-alone ROMS model forced with the
256 WRF winds in un-coupled mode overestimates the cyclone-induced cooling with -2.2°C bias in
257 SST on 13-14 October (Figure 5). The stronger surface winds in stand-alone WRF cause the larger
258 cold bias in stand-alone ROMS model.

259

260 **3.2. Cyclone-induced mixing**

261 The coupled atmosphere-ocean-wave simulation is an ideal tool to understand air-sea
262 exchange of fluxes and their effects on the oceanic water column. Surface wind sets up currents
263 on the surface as well as initiate mixing in the interior of the upper ocean. In order to examine the
264 strength of mixing due to Phailin, the model simulated vertical temperature profile together with

265 the surface wind speed, zonal and meridional components of current, and kinetic energy at the on-
266 track and off-track locations are plotted in Figure 6. Comparatively stronger zonal and meridional
267 currents observed at the off-track location than the on-track location on 12 October. The larger
268 kinetic energy available at the off-track location leads to greater mixing resulting into deeper mixed
269 layer on 12 October as compared to the on-track location. The surface wind speed at the on-track
270 location shows a typical temporal variations of a passing cyclone. The wind speed peaks, drops,
271 and attains second peak as the cyclone approaches, crosses over, and depart the location. The
272 surface currents forced by these large variations in wind speed and direction at the on-track
273 location results into comparatively weaker magnitude than the off-shore location.

274 The thermocline, defined as the depth of maximum temperature gradient, is usually
275 referred to a location dependent isotherm depth (Kessler, 1990; Wang et al, 2000). Over the BoB
276 region, the depth of 23°C isotherm (D23) found to be an appropriate representative depth of the
277 thermocline (Girishkumar et al., 2013). Based on the density criteria, we calculated the oceanic
278 mixed layer depth (MLD) as the depth where density increased by 0.125 kg m^{-3} from its surface
279 value. The inertial mixing introduced by the cyclone play central role in deepening of D23 and
280 MLD on 12th October 2013. The warmer near-surface waters mixed downward when the cyclone
281 crossed over this location. After the passage of cyclone, shoaling of D23 and MLD observed as a
282 consequence of cyclone induced upwelling that entrain colder waters from the thermocline into
283 the mixed layer. The temperature of the upper surface water (25 -30 m) decreased by 3.5°C from
284 its maximum value of 28°C after the landfall of the cyclone on 12-13th October at the off-shore
285 location (Figure 6g). In response to the strong cyclonic winds, the D23 deepening by 40 m (from
286 50 m to 90 m) was observed during 04-12 GMT on 12 October. At the same time, the MLD,
287 denoted by a thick black line in Figure 6g, deepens by about 15 m. On the other hand, the on-track
288 location showed cooling at the surface only for a short time on 13 October and the deepening of
289 D23 and MLD were 20 m and 10 m, respectively. To examine the role of cyclone induced mixing
290 in modulating the thermohaline structure of upper ocean, we carried out further analysis on the
291 coupled model simulations as discussed in the following sections.

292

293 **3.2.1. Kinetic energy distribution**

294 During the initial phase of Phailin, the zonal and meridional currents were primarily
295 westward and southward, respectively (Figures 6c, 6d, 6h, and 6i).. However, on and after 12th
296 October when cyclone attains peak intensity and crosses over the location, alternative temporal
297 sequences of westward/eastward in zonal current and southward/northward in meridional current
298 were noticed in current profiles (Figure 6). The frequency of these reversals in zonal and
299 meridional currents are recognized as near-inertial frequency generated from the storm at these
300 locations. The direction and magnitude of currents represent a variability that corresponds to the
301 presence of near-inertial oscillations at the selected locations. The kinetic energy (KE) of currents
302 at various depths is a proxy of energy available in the water column that becomes conducive to
303 turbulent and inertial mixing. Time series of KE associated with the barotropic and depth-averaged
304 baroclinic components of current at the two point locations are illustrated in Figure 6e (on-track)
305 and 6j (off-track). The KE associated with the baroclinic component found to be much higher than
306 the barotropic component of current at the both on-track and off-shore locations. The depth-
307 averaged baroclinic and barotropic current components' KE also depict the impinging oscillatory
308 behavior. The peak magnitude of KE in baroclinic and barotropic currents at the off-shore location
309 found to be $1.2 \text{ m}^2 \text{ s}^{-2}$ and $0.3 \times 10^{-2} \text{ m}^2 \text{ s}^{-2}$, respectively on 12th October at 08:00 GMT. Whereas
310 the magnitude of KE in baroclinic and barotropic currents at the on-shore location were smaller
311 than the off-shore location during the peak intensity of cyclone. The peak magnitude of kinetic
312 energy in baroclinic current at the off-track location was more than double to that of on-track
313 location. The comparatively smaller magnitude of KE at the on-shore location could be associated
314 with the rapid variations in wind speed and direction leading to complex interaction between
315 subsurface currents in the central region of the cyclone. It is worth noting that the time of peak KE
316 in baroclinic currents coincide with the deepening of MLD and D23. Therefore, the KE generated
317 in NIO is responsible for sub-surface mixing that acts to deepen the mixed layer. The analysis
318 suggests that energy available for mixing process in the water column was mostly confined to the
319 baroclinic currents at various depths.

320

321 **3.2.2. Primary frequency and depth of mixing**

322 The power spectrum analysis was performed on the time series profiles at the two selected
323 locations - to get a distribution of all frequencies operating in the mixing process during the passage

324 of Phailin. The power spectrum analysis performed on the zonal and meridional components of
325 the baroclinic current profile and shown in Figure 7. It is clear from the figure that the tidal (M2,
326 the semidiurnal component of tide) and near-inertial oscillations (f) are the two dominant
327 frequencies on the surface during the cyclone Phailin. Under the influence of cyclonic winds, the
328 NIO signal was stronger ($0.84 \text{ m}^2\text{s}^{-2}$) at the off-track than the on-track location. The depth
329 penetration of NIO was up to 50 m and 35 m at the off-track and on-track location, respectively.
330 The tidal frequency (M2) and inertial frequency (f) bands shown in the Figure 7 implies that the
331 inertial oscillations were dominant over the tidal constituent in zonal and meridional baroclinic
332 currents. At the off-track location, the largest power of the NIO was noticed at 14 m depth but the
333 tidal oscillations were almost absent in the vertical section of baroclinic current (Figure 7). This
334 finding motivated us to analyze the significance and distribution of this sub-surface variability that
335 resulted in an anomalous deepening of MLD. The highest power of this signal at the off-track
336 location was associated within 0-15 m with the magnitude of $0.84 \text{ m}^2 \text{ s}^{-1}$ in zonal baroclinic current
337 and within 0-38 m with the magnitude of $0.76 \text{ m}^2 \text{ s}^{-1}$ in meridional baroclinic current. These
338 signals, however, weaken with increasing depth and almost disappeared around 120 m depth.
339 These NIO were the strongest signals at the 14 m depth in presence of local wind stress that
340 dominated the mixing compared to any other process. Other processes include the background
341 flows, the presence of eddies, variations in sea surface height, non-linear wave-wave and wave-
342 current interactions (Guan et al., 2014; Park and Watts, 2005).

343 The second order butterworth filter was applied on the baroclinic current components in
344 order to get the strength of NIO in the frequency range of 0.028 to 0.038 cycles h^{-1} at the selected
345 locations. The filtered baroclinic current was further utilized to calculate the filtered inertial
346 baroclinic KE (E_f in m^2s^{-2}). The daily profiles of baroclinic KE were analysed at the two selected
347 locations and shown in Figure 8. The peak baroclinic KE differs from $0.14 \text{ m}^2\text{s}^{-2}$ at the on-track to
348 $0.23 \text{ m}^2\text{s}^{-2}$ at the off-track location on 12 October. As shown in Figures 6 and 7, the filtered
349 baroclinic KE profiles (Figure 8) confirm the dominant presence of NIO at the off-track location
350 as compared to the on-track location. The decay of NIO with the increasing depth was noticed at
351 both the locations. However, the NIO baroclinic KE penetrated up to 80 m in case of off-track as
352 compared to only 50 m at the on-track location. The analysis, therefore, suggests that the NIO
353 generated during the Phailin were more energetic at the selected off-track location, which was also
354 the location of maximum surface cooling as noticed in Figure 5. Therefore, the further analysis in

355 the subsequent sections is limited to the off-track location only. In order to analyze the time
356 distribution of the strong NIO, wavelet transform analysis was applied on the zonal and meridional
357 baroclinic currents at 14 m depth. The Scalogram, shown in Figure 9, depicts the generation of
358 NIO signal at the off-track location on 12th October that subsequently got strengthen and attains
359 its peak value on the mid of 13th October. The energy percentage of the meridional component was
360 always lower than the zonal component. The peak values of energy percentage was found in the
361 time periods between 1-1.3 days.

362 **3.2.3. Role of downward propagation of energy**

363 To investigate the energy propagation from the surface to the interior layers of upper-
364 ocean, we derived the rotary spectra (Gonella, 1972; Hayashi, 1979) of near-inertial wave numbers
365 and shown in Figure10. The daily averaged vertical wave-number rotary spectra provides a clear
366 picture of wind energy distribution in the sub-surface water. The anticyclonic spectrum (A_m) is
367 dominating over the cyclonic spectra (C_m) for the entire duration of the cyclone. This feature
368 indicates that the energy is propagating downward generated by these inertial oscillations. The
369 magnitude of these oscillations increased from initial stage up to 12th October and remained at high
370 energy density for the rest of the cyclone period. This downward directed energy initiated a process
371 of mixing between the mixed layer and the thermocline. This energy helps to deepen the mixed
372 layer against oceanic stratification by introducing a strong shear. The buoyancy of stratified ocean
373 was overcome to some extent by the shear generated that assist in mixing process during the very
374 severe cyclone. Alford and Gregg (2001) highlighted that in most of the cases, the energy of inertial
375 oscillations potentially penetrates the mixed layer but suddenly drops down as it touches the
376 thermocline. The energy dissipation mechanism studied in few other studies (Chant, 2001; Jacob,
377 2003).The 2-layer model described by Burchard and Rippeth (2009) illustrated the process of
378 generation of sufficient shear to start mixing near the thermocline. Their simple model ignored the
379 effect of the lateral density gradient, mixing, and advection. Burchard et al. (2009) mentioned four
380 important parameters for the shear generation, i.e. surface wind stress ($P_s S^2$), bed stress ($-D_b S^2$),
381 interfacial stress ($-D_i S^2$), and barotropic flow ($P_m S^2$). Utilizing simulations from our coupled
382 atmosphere-ocean-wave model, we calculated individual terms as suggested by Burchard et al.
383 (2009) and presented in Figure 10. Surface wind stress found to be the most dominating term in

384 modulating the magnitude of bulk shear during the stormy event. Rest of the terms were relatively
385 weaker and, therefore, contributing only marginally to the variability of the bulk shear.

386 To examine the generation and dissipation of these inertial oscillations, the shear generated
387 by the near-inertial baroclinic current (S_f^2) and turbulent kinetic energy dissipation rate (ϵ) were
388 calculated and analyzed. The shear produced by inertial oscillations increased at 20-80 m depth
389 and higher magnitude was associated with peak wind speed of cyclone (Figure 12a). This shear
390 overcome the stratification (Figure 12b), represented by buoyancy frequency N^2 , and played
391 important role in mixing and deepening of the thermocline and mixed layer on 12th October. The
392 value of kinetic energy dissipation rate (ϵ) increased from 4×10^{-14} to 2.5×10^{-13} W kg^{-1} on
393 approaching the thermocline (Figure 12c). The increase in ϵ indicates the weakening of the shear
394 generated by the inertial waves leading to the fast disappearance of these baroclinic instabilities
395 from the region. The non-linear interaction between the NIO and internal tides together with the
396 prevailing background currents cause rapid dissipation of kinetic energy in the thermocline. Guan
397 et al. (2014) also reported an accelerated dampening of NIO associated with the wave-wave
398 interactions between NIO and internal tides. The background currents found to modify the
399 propagation of NIO (Park and Watts, 2005). The magnitude of the turbulent eddy diffusivity (K_ρ),
400 shown in Figure 12d, implies that the greater mixing takes place within the mixed layer where
401 K_ρ was high (6.3×10^{-11} to 1.2×10^{-11} $\text{m}^2 \text{s}^{-1}$). The daily averaged values of ϵ and K_ρ were 1.2×10^{-13}
402 W kg^{-1} and 1.5×10^{-10} $\text{m}^2 \text{s}^{-1}$, respectively on 12th October, which were higher as compared to
403 the initial two days of the cyclonic event. Results from the present study, as well as the conclusions
404 from the past studies, indicate that wave-current interaction, mesoscale processes, and wave-wave
405 interaction can affect the process of downward mixing and cause the dissipation of inertial
406 oscillations.

407

408 **4. Conclusions**

409 Processes controlling the sub-surface mixing were evaluated under the high wind speed
410 regime of a severe cyclonic storm Phailin over the BoB. A coupled atmosphere-ocean-wave
411 (WRF+ROMS+SWAN) model as part of the COAWST modeling system was used to simulate
412 atmospheric and oceanic conditions during the passage of Phailin cyclone. A detailed analysis of

413 model simulated data revealed interesting features of generation, propagation, and dissipation of
414 kinetic energy in the upper oceanic water column. Deepening of the MLD and thermocline by 15
415 m and 40 m, respectively were explained through the strong shear generated by the inertial
416 oscillations that helped to overcome the stratification and initiate mixing at the base of the mixed
417 layer. However, there was a rapid dissipation of the shear with increasing depth below the
418 thermocline. The peak magnitude of kinetic energy in baroclinic and barotropic currents found to
419 be $1.2 \text{ m}^2 \text{ s}^{-2}$ and $0.3 \times 10^{-2} \text{ m}^2 \text{ s}^{-2}$, respectively. The power spectrum analysis suggested a dominant
420 frequency operative in sub-surface mixing that was associated with near-inertial oscillations. The
421 peak strength of $0.84 \text{ m}^2 \text{ s}^{-1}$ in the zonal baroclinic current found at 14 m depth at a location in
422 northwestern BoB. The baroclinic kinetic energy remains higher ($> 0.03 \text{ m}^2 \text{ s}^{-2}$) during 11-12
423 October and decreased rapidly thereafter. The wave-number rotary spectra identified the
424 downward propagation, from the surface up to the thermocline, of energy generated by inertial
425 oscillations. A quantitative analysis of shear generated by the near-inertial baroclinic current
426 showed higher shear generation at 20-80 m depth during peak surface winds. Analysis highlights
427 that greater mixing within the mixed layer takes place where the eddy kinetic diffusivity was high
428 ($> 6 \times 10^{-11} \text{ m}^2 \text{ s}^{-1}$). The turbulent kinetic energy dissipation rate increased from 4×10^{-14} to 2.5×10^{-13}
429 W kg^{-1} on approaching the thermocline that dampened mixing process further down into the
430 thermocline layer. The wave-current interaction, mesoscale processes, and wave-wave interaction
431 increased the dissipation rate of shear and, thereby, limited the downward mixing up to the
432 thermocline. The coupled model found to be a useful tool to investigate air-sea interaction, kinetic
433 energy propagation, and mixing in the upper-ocean. The results from this study highlight the
434 importance of atmosphere-ocean coupling for better understanding of oceanic response under the
435 strong wind conditions. The proper representation of kinetic energy propagation and oceanic
436 mixing have applications in improving the intensity prediction of cyclone, storm surge forecasting,
437 and biological productivity.

438

439 **Author contribution:** KRP and TN performed model simulations and analyzed data. VP prepared
440 the manuscript with contributions from all co-authors.

441

442

443 **Acknowledgements**

444 ECCO2 is a contribution to the NASA Modeling, Analysis, and Prediction (MAP)
445 program. The study benefitted from the funding support from Ministry of Earth Sciences, Govt. of
446 India and Space Applications Centre, Indian Space Research Organisation. High Performance
447 Computing (HPC) facility provided by IIT Delhi and Department of Science and Technology
448 (DST), Govt. of India are thankfully acknowledged. Authors are thankful to Dr. Lingling Xie for
449 his productive suggestions. Graphics generated in this manuscript using Ferret and NCL. TN and
450 KRP acknowledge MoES and UGC-CSIR, respectively for their doctoral fellowship support.

451

452 **References**

453 Alam, M. M., Hossain, M.A. and Shafee, S.: Frequency of Bay of Bengal cyclonic storms and
454 depressions crossing different coastal zones, *Int. J. Climatol.*, 23, 1119–1125,
455 doi:10.1002/joc.927, 2003.

456 Alford, M.H., Gregg, M.C.: Near-inertial mixing: modulation of shear, strain and microstructure
457 at low latitude. *J. Geophys. Res.* 106 (C8), 16947–16968, 2001.

458 Auger F., Flandrin, P.: Improving the Readability of Time-Frequency and Time-Scale
459 Representations by the Reassignment Method. *IEEE Transactions on Signal Processing.* 43,
460 1068–1089, 1995.

461 Booij, N., Ris, R. C., and Holthuijsen, L. H.: A third-generation wave model for coastal regions,
462 Part I, Model description and validation, *J. Geophys. Res.*, 104(C4), 7649–7666,
463 doi:10.1029/98JC02622, 1999.

464 Burchard, H., Rippeth, T.P.: Generation of bulk shear spikes in shallow stratified tidal seas. *J.*
465 *Phys. Oceanogr.* 39, 969–985, 2009.

466 Chang, S. W., and Anthes, F.A.: The mutual response of the tropical cyclone and the ocean. *J.*
467 *Phys. Oceanogr.*, 9, 128–135, 1979.

468 Chant, R.J.: Evolution of near-inertial waves during an upwelling event on the New Jersey Inner
469 Shelf. *J. Phys. Oceanogr.* 31, 746–764, 2001.

470 Chen, S., Chen, D., Xing, J.: A study on some basic features of inertial oscillations and near-inertial
471 internal waves. *Ocean Science*, 13 (5), 829-836, 2017.

472 Chassignet, E.P., Arango, H.G., Dietrich, D., Ezer, T., Ghil, M., Haidvogel, D.B., Ma, C.C.,
473 Mehra, A., Paiva, A.M., Sirkes, Z.: DAMEE-NAB: the base experiments. *Dyn. Atmos. Oceans*
474 32, 155–183, 2000.

475 Cione, J. J., and Uhlhorn, E.W.: Sea surface temperature variability in hurricanes: Implications
476 with respect to intensity change, *Mon. Weather Rev.*, 131, 1783–1796, doi:10.1175//2562.1,
477 2003.

478 Dudhia, J.: Numerical study of convection observed during the winter monsoon experiment using
479 a mesoscale two dimensional model. *J Atmos Sci.* 46, 3077–3107, 1989.

480 Gill, A. E.: On the behavior of internal waves in the wake of storms, *J. Phys. Oceanogr.*, 14, 1129
481 – 1151, 1984.

482 Girishkumar, M. S., Ravichandran, M., Han, W.: Observed intraseasonal thermocline variability
483 in the Bay of Bengal. *J. Geophys. Res. Oceans*, 118, 3336–3349, doi:10.1002/jgrc.20245, 2013.

484 Gonella, J.: A study of inertial oscillations in the upper layers of the oceans. *Deep-Sea Res.*, 18,
485 775–788, 1971.

486 Gonella, J.: A rotary-component method for analysing meteorological and oceanographic vector
487 time series. *Deep-Sea Research* 19, 833–846, 1972.

488 Guan, S., Zhao, W., Huthnance, J. Tian, J., and Wang, J.: Observed upper ocean response to
489 typhoon Megi (2010) in the Northern South China Sea. *J. Geophys. Res. Oceans*, 119, 3134–
490 3157, doi:10.1002/2013JC009661, 2014.

491 Haidvogel, D.B., Arango, H.G., Budgell, W.P., Cornuelle, B.D., Curchitser, E., Di Lorenzo, E.,
492 Fennel, K., Geyer, W.R., Hermann, A.J., Lanerolle, L., Levin, J., McWilliams, J.C., Miller,
493 A.J., Moore, A.M., Powell, T.M., Shchepetkin, A.F., Sherwood, C.R., Signell, R.P., Warner,
494 J.C., Wilkin, J.: Regional ocean forecasting in terrain-following coordinates: model formulation
495 and skill assessment. *Journal of Computational Physics* 227, 3595–3624, 2008.

496 Haidvogel, D.B., Arango, H.G., Hedstrom, K., Beckmann, A., Malanotte-Rizzoli, P.
497 Shchepetkin, A.F.: Model evaluation experiments in the North Atlantic Basin: Simulations in
498 nonlinear terrain-following coordinates. *Dyn Atmos Oceans* 32, 239–281, 2000.

499 Hayashi, Y.: Space-time spectral analysis of rotary vector series. *J. Atmos. Sci.* 36 (5), 757–766,
500 1979.

501 Hong, S.Y., Lim, J.O.J.: The WRF single-moment 6-class microphysics scheme (WSM6). *J*
502 *Korean Meteor Soc* 42:2, 129-151, 2006.

503 IMD Report.: Very Severe Cyclonic Storm, PHAILIN over the Bay of Bengal (08-14 October
504 2013) A Report. India Meteorological Department, Technical Report, October 2013.

505 Jacob, S.D., Shay, L.K.: The role of oceanic mesoscale features on the tropical cyclone-induced
506 mixed layer response: A case study. *J. Phys. Oceanog.*, 33, 649- 676, 2003.

507 Jacob, R., Larson, J., Ong, E.: M x N Communication and Parallel Interpolation in CCSM Using
508 the Model Coupling Toolkit. Preprint ANL/MCSP1225-0205. Mathematics and Computer
509 Science Division, Argonne National Laboratory, 25 pp, 2005.

510 Johnston, T.M.S., Chaudhuri, D., Mathur, M., Rudnick, D.L., Sengupta, D., Simmons, H.L.,
511 Tandon, A., and Venkatesan, R.: Decay mechanisms of near-inertial mixed layer oscillations in
512 the Bay of Bengal, *Oceanography*, 29(2): 180–191, doi:10.5670/oceanog.2016.50, 2016.

513 Kain, J.S.: The Kain-Fritsch convective parameterization: An update. *J Appl Meteor* 43, 170–
514 181, 2004.

515 Kessler, W. S.: Observations of long Rossby waves in the northern tropical Pacific. *J. Geophys.*
516 *Res.*, 95, 5183–5217, 1990.

517 Kirby, J. T., and Chen T.M.: Surface waves on vertically sheared flows Approximate dispersion
518 relations. *J. Geophys. Res.*, 94(C1),1013–1027, doi:10.1029/JC094iC01p01013, 1989.

519 Komen, G.J., Hasselmann, S., and Hasselmann, K.: On the existence of a fully developed wind-
520 sea spectrum. *J. Phys. Oceanogr.*, 14, 1271–1285. 1984.

521 Kumar VS, Nair A.M.: Inter-annual variations in wave spectral characteristics at a location off the
522 central west coast of India. *Ann Geophys* 33:159–167, doi:10.5194/angeo-33-159, 2015.

523 Leipper, D. F.: Observed Ocean Conditions and Hurricane Hilda, 1964, *J. Atmos. Sci.*, 24, 182–
524 186, doi:10.1175/1520-0469(1967)0242.0.CO;2, 1967.

525 Zhi, Li., Yu, W., Li, T., Murty, V.S.N., and Tangang, F.: Bimodal character of cyclone climatology
526 in the Bay of Bengal modulated by monsoon seasonal cycle. *J Climate* 26:1033-1046. doi:
527 10.1175/JCLI-D-11-00627.1, 2013.

528 Lilly, J. M., Olhede, S. C.: Generalized Morse Wavelets as a Superfamily of Analytic Wavelets.
529 *IEEE Transactions on Signal Processing*. 60 (11), 6036–6041, 2012.

530 Longshore, D.: *Encyclopedia of Hurricanes, Typhoons, and Cyclones*, 468 pp., Checkmark, New
531 York, 2008.

532 Larson, J., Jacob, R., Ong, E.: The Model Coupling Toolkit: A New Fortran90 Toolkit for
533 Building Multiphysics Parallel Coupled Models. Preprint ANL/MCS- P1208-1204.
534 Mathematics and Computer Science Division, Argonne National Laboratory, 25 pp, 2004.

535 Lukas, R., and Lindstrom, E.: The mixed layer of the western equatorial Pacific Ocean, *J. Geophys.*
536 *Res.*, 96, 3343–3357, 1991.

537 MacKinnon, J.A., Gregg, M.C.: Spring Mixing: Turbulence and Internal Waves during
538 Restratification on the New England Shelf. *Journal of Physical Oceanography*. 35:12, 2425-
539 2443 2005.

540 Mandal M., Singh K. S., Balaji M., Mohapatra M.: Performance of WRF-ARW model in real-
541 time prediction of Bay of Bengal cyclone ‘Phailin’. *Pure Appl. Geophys* DOI 10.1007/s00024-
542 015-1206-7, 2015.

543 Menemenlis, D., et al., NASA supercomputer improves prospects for ocean climate research, *Eos*
544 *Trans. AGU*, 86(9), 89–96, doi:10.1029/2005EO090002, 2005.

545 Monin, A.S., Obukhov, A.M.F.: Basic laws of turbulent mixing in the surface layer of the
546 atmosphere. *Contrib Geophys Inst Acad Sci USSR* 151:163, e187, 1954.

547 National Centers for Environmental Prediction/National Weather Service/NOAA/U.S.
548 Department of Commerce: NCEP FNL Operational Model Global Tropospheric Analyses,
549 continuing from July 1999. Research Data Archive at the National Center for Atmospheric

550 Research, Computational and Information Systems Laboratory. Dataset.
551 <https://doi.org/10.5065/D6M043C6>, 2000.

552 National Geophysical Data Center. 2-minute Gridded Global Relief Data (ETOPO2) v2. National
553 Geophysical Data Center, NOAA. doi:10.7289/V5J1012Q, 2006.

554 Neetu, S., Lengaigne, M., Vincent, E.M., Vialard, J., Madec, G., Samson, G., Ramesh Kumar,
555 M.R., and Durand, F.: Influence of upper-ocean stratification on tropical cyclone-induced
556 surface cooling in the Bay of Bengal, *J. Geophys. Res.*, 117, C12020,
557 doi:10.1029/2012JC008433, 2012.

558 Noh, Y., Cheon, W.G., Hong, S.Y., Raasch, S.: Improvement of the K-profile model for the
559 planetary boundary layer based on large eddy simulation data. *Bound Layer Meteor* 107, 401–
560 427, 2003.

561 Osborn, T.R.: Estimates of the Local-Rate of Vertical Diffusion from Dissipation Measurements.
562 *J. Phys. Oceanogr.* 10, 83–89, 1980.

563 Palmer, M.R., Rippeth, T.P., Simpson, J. H.: An investigation of internal mixing in a seasonally
564 stratified shelf sea. *J. Geophys. Res.* 113, C12005, doi:10.1029/2007JC004531, 2008.

565 Pant V, Girishkumar M.S., Udaya Bhaskar T.V.S., Ravichandran M., Papa F., Thangaprakash
566 V.P.: Observed interannual variability of near-surface salinity in the Bay of Bengal, *J. Geophys.*
567 *Res* 120(5):3315–3329, 2015.

568 Park, J.H., and Watts, D. R.: Near-inertial oscillations interacting with mesoscale circulation in the
569 southwestern Japan/East Sea. *Geophys. Res. Lett.*, 32, L10611, doi: 10.1029/2005GL022936,
570 2005.

571 Prakash K.R., Vimlesh Pant: Upper oceanic response to tropical cyclone Phailin in the Bay of
572 Bengal using a coupled atmosphere-ocean model, *Ocean Dynamics*, 67, 51-64,
573 doi:10.1007/s10236-016-1020-5, 2017.

574 Price, J. F., Mooers, C.N., and Van Leer, J.C.: Observation and simulation of storm-induced
575 mixed-layer deepening. *J. Phys. Oceanogr.*, 8, 582-599, [https://doi.org/10.1175/1520-
576 0485\(1978\)008<0582:OASOSI>2.0.CO;2](https://doi.org/10.1175/1520-0485(1978)008<0582:OASOSI>2.0.CO;2), 1978.

577 Price, J.F.: Upper ocean response to a hurricane. *J. Phys. Oceanogr.*, 11, 153-175, 1981.

578 Rao, R. R., and Sivakumar, R.: Seasonal variability of sea surface salinity and salt budget of the
579 mixed layer of the north Indian Ocean, *J. Geophys. Res.*, 108(C1), 3009,
580 doi:10.1029/2001JC000907, 2003.

581 Sanford, T. B., Black, P.G., Haustein, J., Feeney, J.W., Forristall, G.Z., and Price, J.F.: Ocean
582 response to a hurricane. Part I: Observations. *J. Phys. Oceanogr.*, 17, 2065–2083, 1987.

583 Schahinger, R.B.: Near inertial motion on the south Australian shelf. *J. Phys. Oceanogr.*, 18(3),
584 492-504, 1988.

585 Shchepetkin and A. F., McWilliams J. C.: The Regional Ocean Modeling System: A split-explicit,
586 free-surface, topography following coordinates ocean model, *Ocean Modelling*, 9, 347-404,
587 2005.

588 Skamarock, W.C., Klemp, J.B., Dudhia, J., Gill, D.O., Barker, D.M., Wang, W., Powers, J.G.: A
589 Description of the Advanced Research WRF Version 2. NCAR Technical Note, NCAR/TN-
590 468+STR., 2005.

591 Shay, L. K., Black, P., Mariano, A., Hawkins, J., and Elsberry, R.: Upper ocean response to
592 hurricane Gilbert, *J. Geophys. Res.*, 97(20), 227–248, 1992.

593 Shay, L. K. and Elsberry, R.L.: Vertical structure of the ocean current response to a hurricane. *J.*
594 *Phys. Oceanogr.*, 19, 649-669, 1989.

595 Shay, L. K., Goni, G.J., and Black, P.G.: Effects of a warm oceanic feature on Hurricane Opal,
596 *Mon. Weather Rev.*, 128, 1366–1383, doi:10.1175/1520-0493(2000)1282.0.CO;2, 2000.

597 Shearman, R.K.: Observations of near-inertial current variability on the New England shelf. *J.*
598 *Geophys. Res.* 110, C02012, doi:10.1029/2004JC002341, 2005.

599 Srinivas, C. V., Mohan, G. M., Naidu, C. V., Baskaran, R., Venkatraman B. :Impact of air-sea
600 coupling on the simulation of tropical cyclones in the North Indian Ocean using a simple 3-D
601 ocean model coupled to ARW, *J. Geophys. Res. Atmos.*, 121, 9400,9421,
602 doi:10.1002/2015JD024431, 2016.

603 Suzana, J Carmargo, Adam H Sobel, Anthony G Barnston and Kerry A. Emanuel: Tropical
604 cyclone genesis potential index in climate models. *Tellus* 59A:428-443, 2007.

605 Taylor, P.K., Yelland, M.J.: The dependence of sea surface roughness on the height and steepness
606 of the waves. *J. Phys. Oceanogr.*, 31, 572–590, 2001.

607

608 Thadathil, P., Muraleedharan, P.M., Rao, R.R., Somayajulu, Y.K., Reddy, G.V., and
609 Revichandran, C.: Observed seasonal variability of barrier layer in the Bay of Bengal, *J.*
610 *Geophys. Res.*, 112, C02009, doi:10.1029/2006JC003651, 2007.

611 Varkey, M. J., Murty, V.S.N., and Suryanarayana, A.: Physical oceanography of the Bay of Bengal
612 and Andaman Sea, *Oceanogr. Mar. Biol.*, 34, 1–70, 1996.

613 van der Lee, E.M., and Umlauf, L.: Internal wave mixing in the Baltic Sea: near-inertial waves in
614 the absence of tides. *J. Geophys. Res.* 116, C10016, doi:10.1029/2011JC007072, 2011.

615 Vinayachandran, P. N., Murty, V.S.N., and Ramesh Babu V.: Observations of barrier layer
616 formation in the Bay of Bengal during summer monsoon, *J. Geophys. Res.*, 107(C12), 8018,
617 doi:10.1029/2001JC000831, 2002.

618 Vissa, N.K., Satyanarayana, A.N.V. and Prasad Kumar, B.: Intensity of tropical cyclones during
619 pre- and post-monsoon seasons in relation to accumulated tropical cyclone heat potential over
620 Bay of Bengal, *Nat Hazards* 68: 351. <https://doi.org/10.1007/s11069-013-0625-y>. 2013.

621 Wang, B., Wu, R., and Lukas R.: Annual adjustment of the thermocline in the tropical Pacific
622 Ocean, *J. Clim.*, 13, 596–616, 2000.

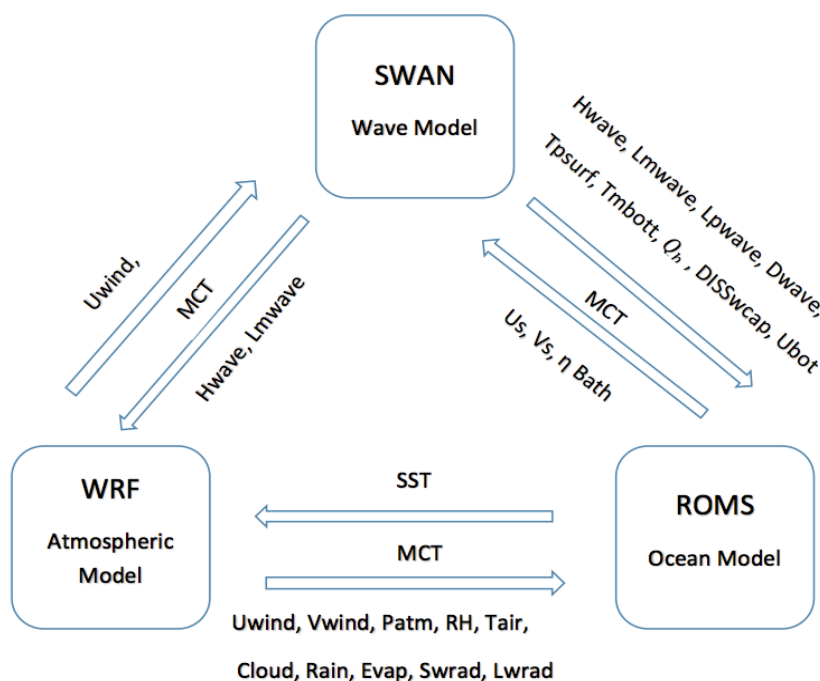
623 Warner, J. C., Sherwood, C.R., Arango, H.G., and Signell, R.P.: Performance of four turbulence
624 closure models implemented using a generic length scale method, *Ocean Modell.*, 8, 81–113,
625 doi:10.1016/j. ocemod.2003.12.003, 2005.

626 Warner, J.C., Armstrong B., He R., Zambon J.B.: Development of a coupled ocean–
627 atmosphere–wave–sediment transport (COAWST) modeling system. *Ocean modelling* 35:230–
628 244. doi:10.1016/j. oceanmod.2010.07.010, 2010.

629 Yanase, W., Satosh, M., Taniguchi, H., and Fujinami, H.: Seasonal and Intraseasonal Modulation
 630 of tropical cyclogenesis environment over the Bay of Bengal during the extended summer
 631 monsoon. *J Climate* 25:2914-2930. doi: 10.1175/JCLI-D-11-00208.1, 2012.

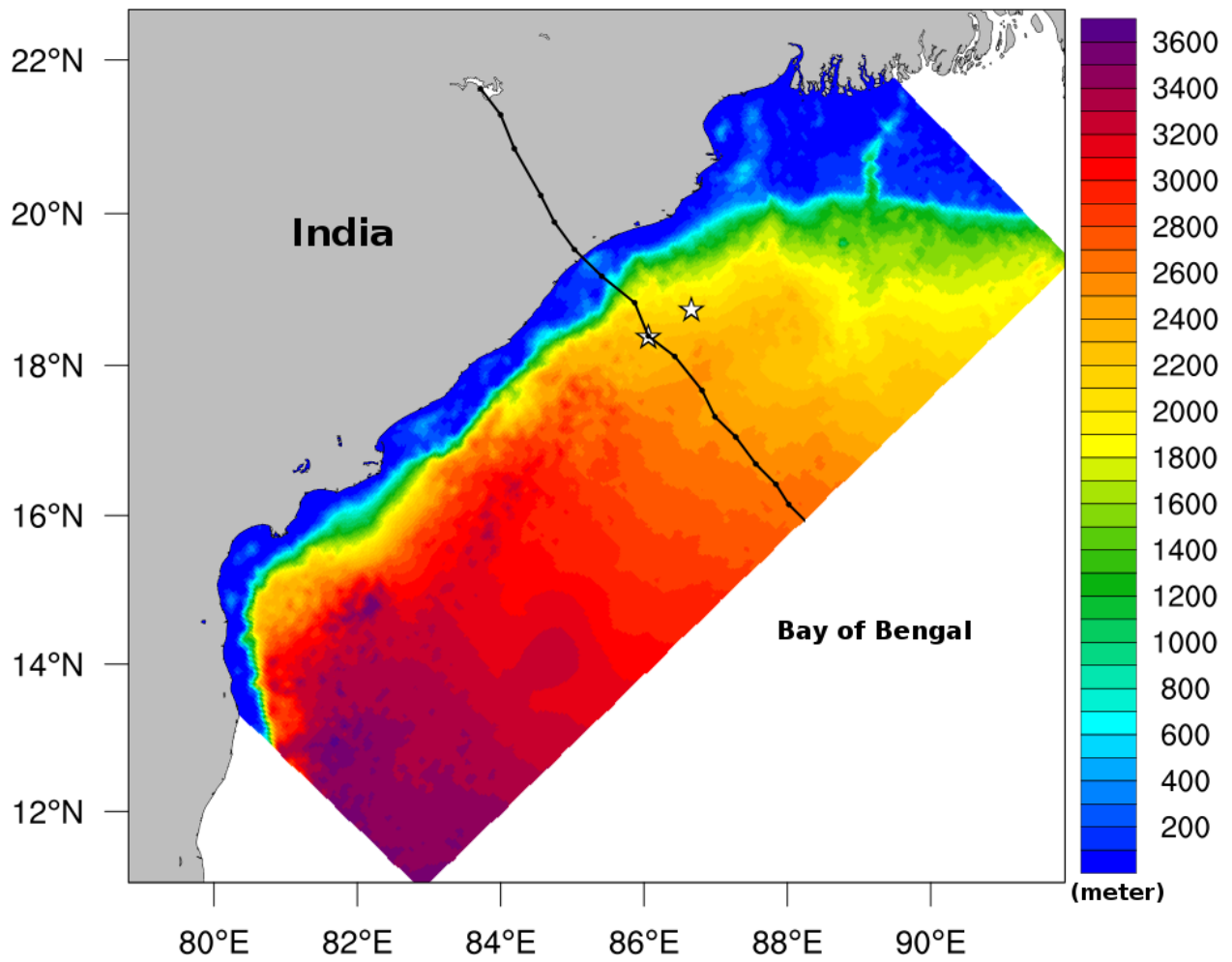
632 Zhang, S., Xie, L., Hou, Y., Zhao, H., Qi, Y., & Yi, X.: Tropical storm-induced turbulent mixing
 633 and chlorophyll-a enhancement in the continental shelf southeast of Hainan Island. *Journal of*
 634 *Marine Systems*, 129, 405-414, 2014.

635
 636
 637
 638
 639



640
 641 **Figure 1:-The block diagram showing the component models WRF, ROMS, and SWAN of the**
 642 **COAWST modeling system together with the variables exchanged among the models. MCT- the**
 643 **model coupling toolkit is a model coupler used in the COAWST system.**

644
 645
 646



647

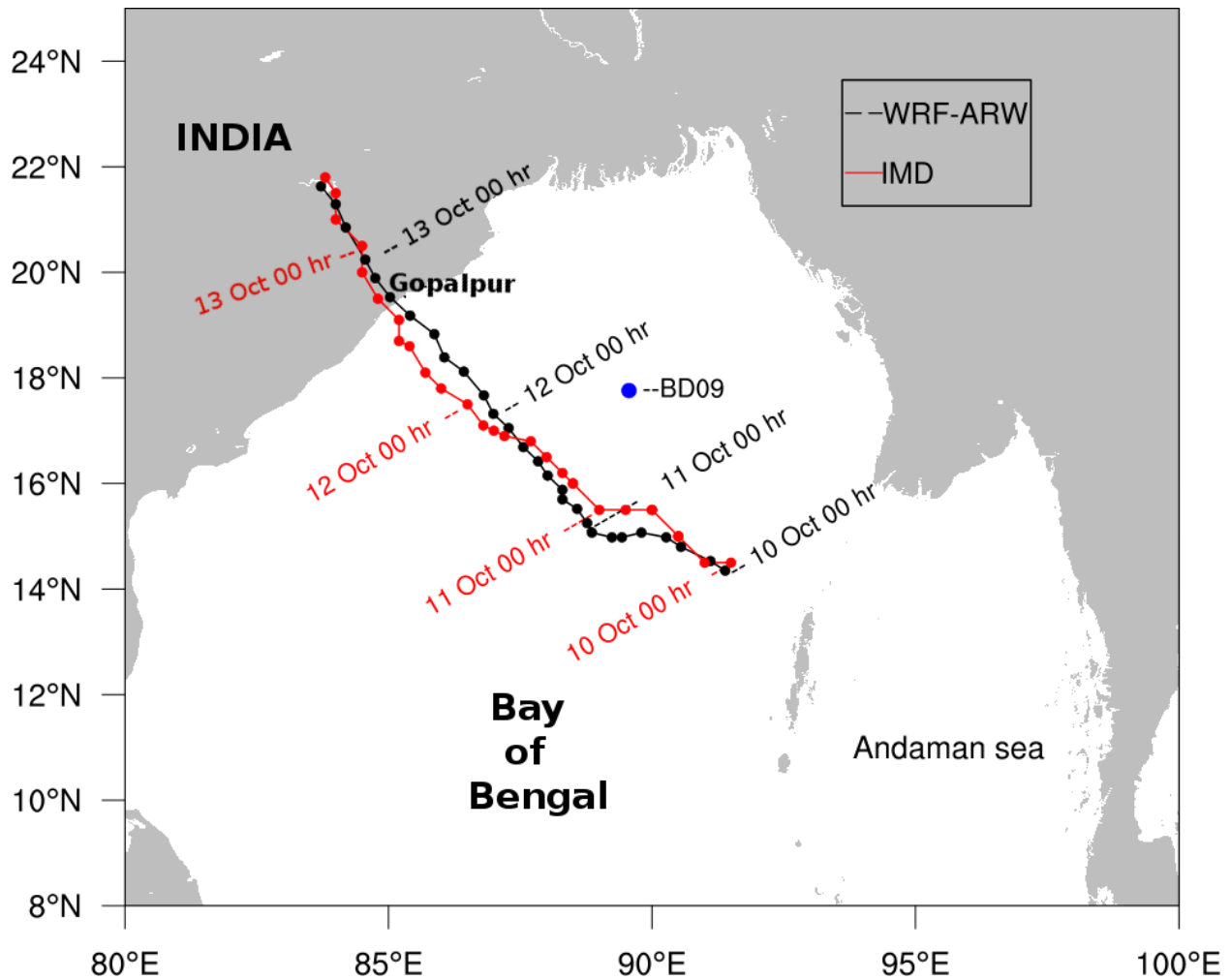
648 **Figure 2:-COAWST model domain (65°-105 °E, 1°-34 °N) overlaid with GEBCO bathymetry (m).**
 649 **Locations used for time-series analysis are marked with stars.**

650

651

652

653



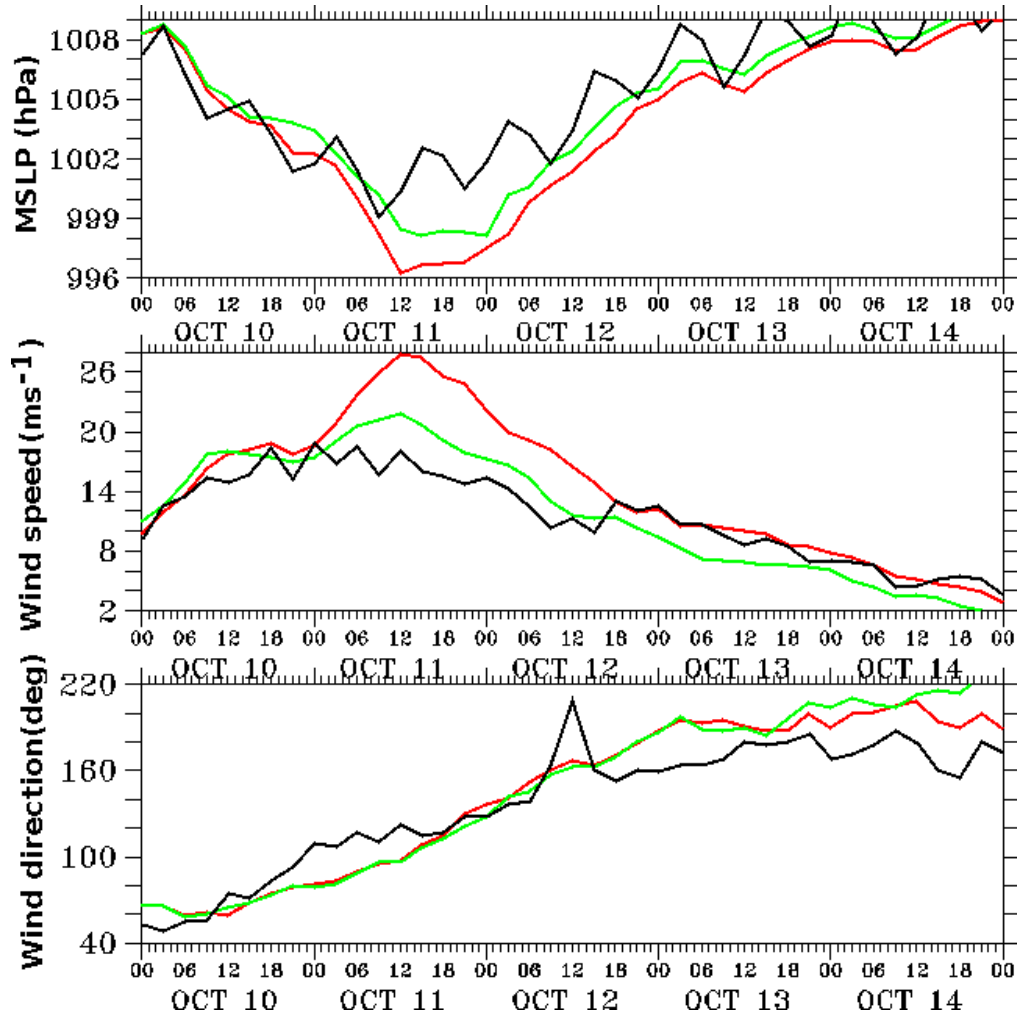
654

655 **Figure 3:- Tracks of Phailin simulated by the coupled model (black) and IMD reported (red). The**
 656 **3-hourly positions of the center of Phailin marked with solid circles and the daily position at 00 hr**
 657 **are labelled with the dates. Location of buoy BD09 is marked with a blue circle.**

658

659

660

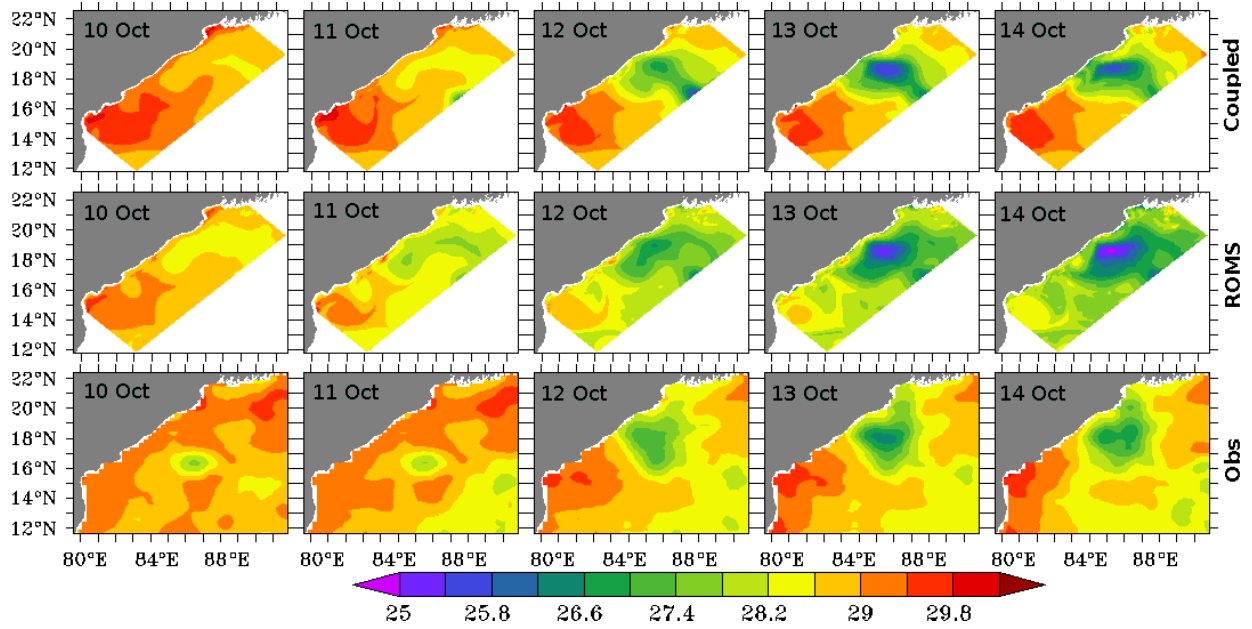


661

662 Figure 4: Comparison of coupled model (green), stand-alone WRF model (red), and observations from a
663 buoy BD09 (black) for the (top panel) mean sea level pressure (hPa), (middle panel) wind speed (ms^{-1}),
664 and (bottom panel) wind direction (degree).

665

666

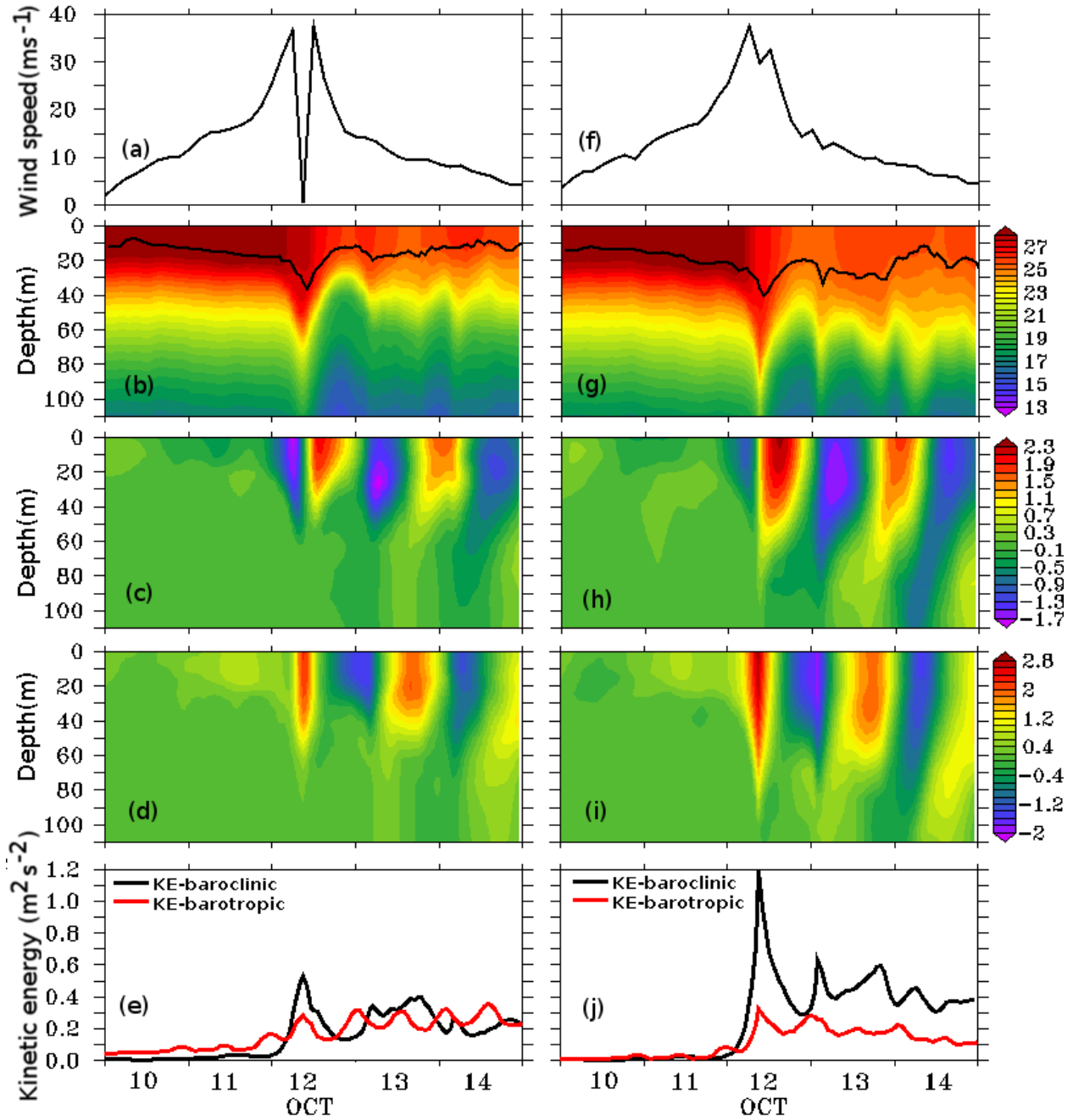


667

668 **Figure 5:- The daily averaged sea surface temperature (SST) in °C simulated by the coupled model**
 669 **(upper panel), stand alone ROMS model (middle panel), and observed from AVHRR sensor on the**
 670 **satellite (lower panel)..**

671

672



673

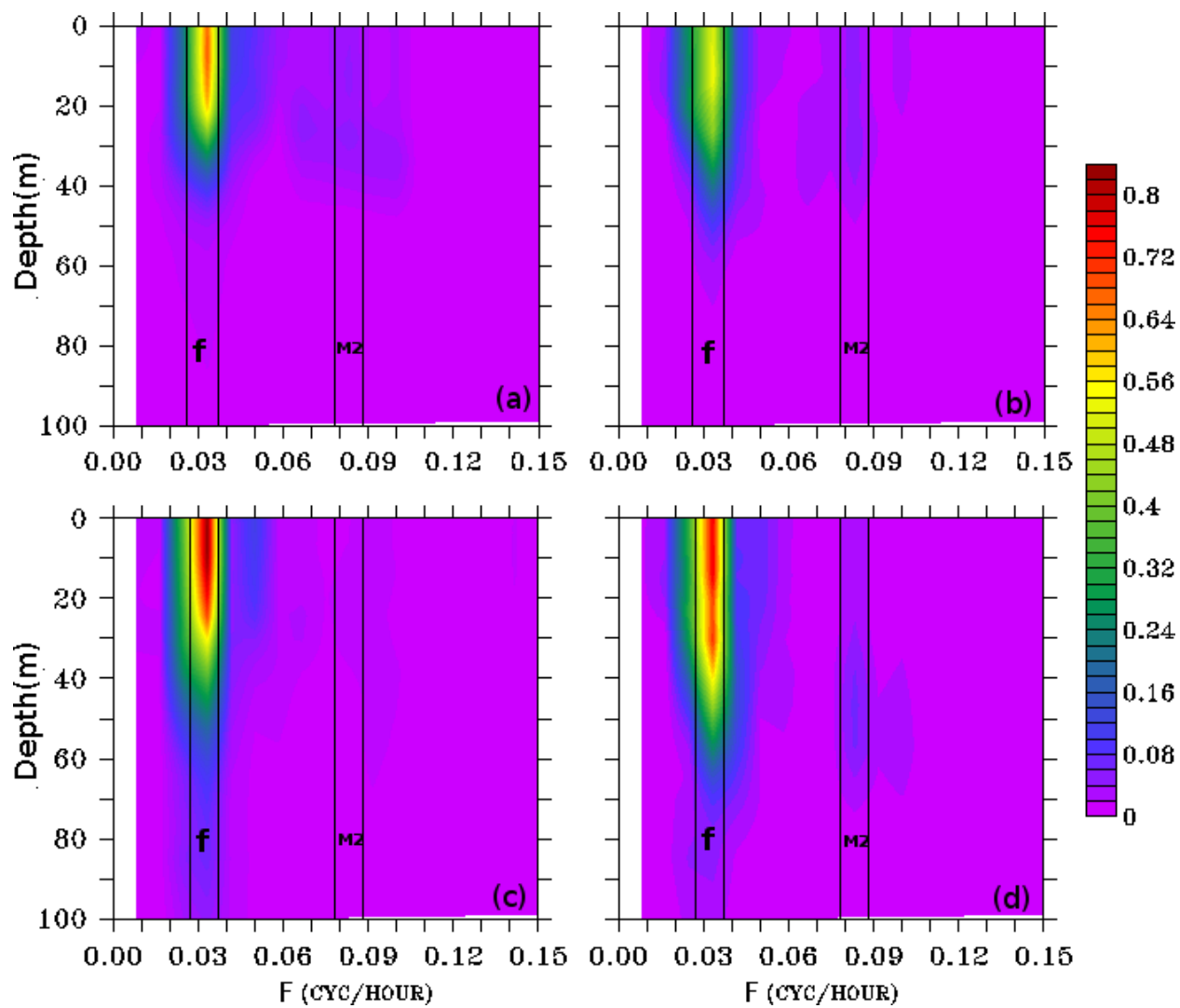
674 **Figure 6: Coupled model simulated and diagnosed variables at the on-track (left panel) and off-**
 675 **track (right panel) locations. (a, f) Surface wind speed (ms^{-1}), (b, g) temperature profile ($^{\circ}\text{C}$) and**
 676 **mixed layer depth (black line), (c, h) u-component of current (ms^{-1}), (d, i) v-component of current**
 677 **(ms^{-1}), (e, j) Kinetic energy of baroclinic (m^2s^{-2}) and barotropic ($\times 10^{-2} \text{m}^2\text{s}^{-2}$) current.**

678

679

680

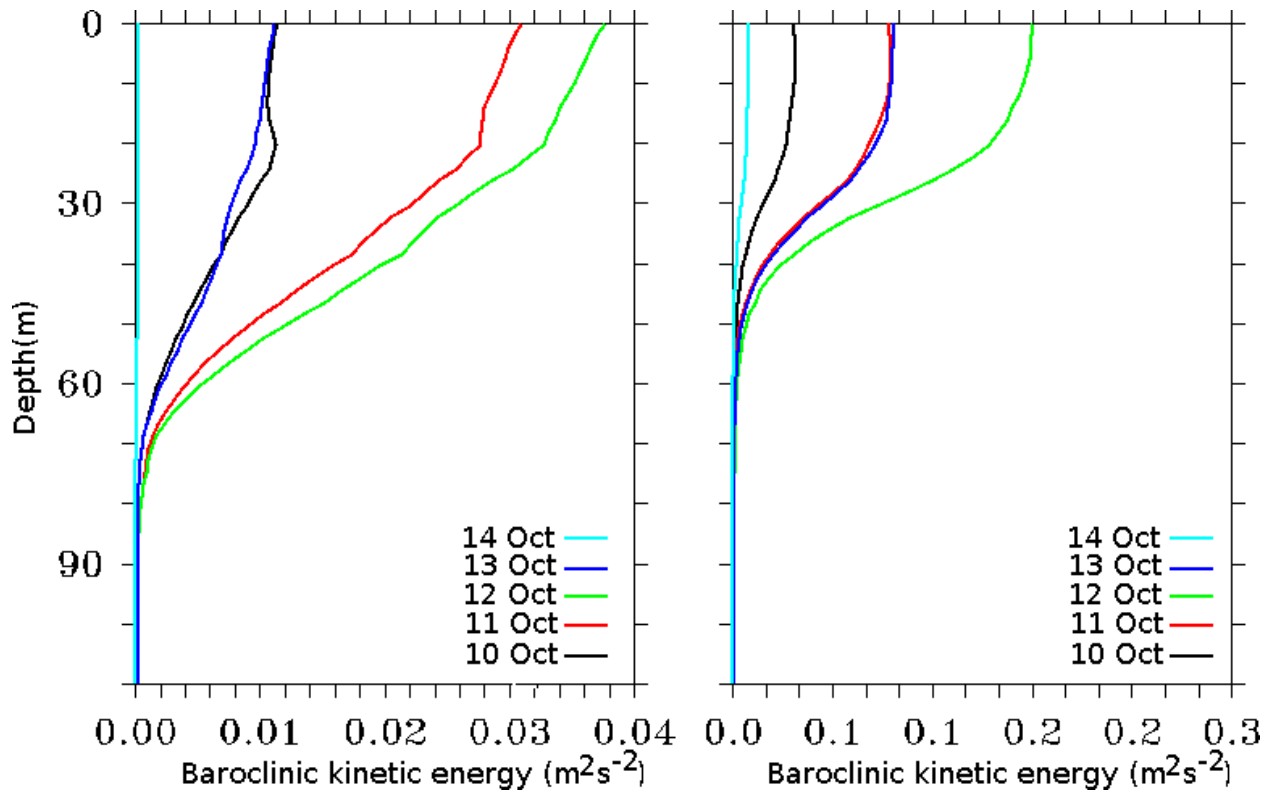
681



682

683 **Figure 7:- The power spectrum analysis (m^2s^{-1}) performed on the simulation period at the on-track**
684 **(upper panel) and off-track (lower panel) locations for (a, c) baroclinic zonal current and (b, d)**
685 **baroclinic meridional current.**

686

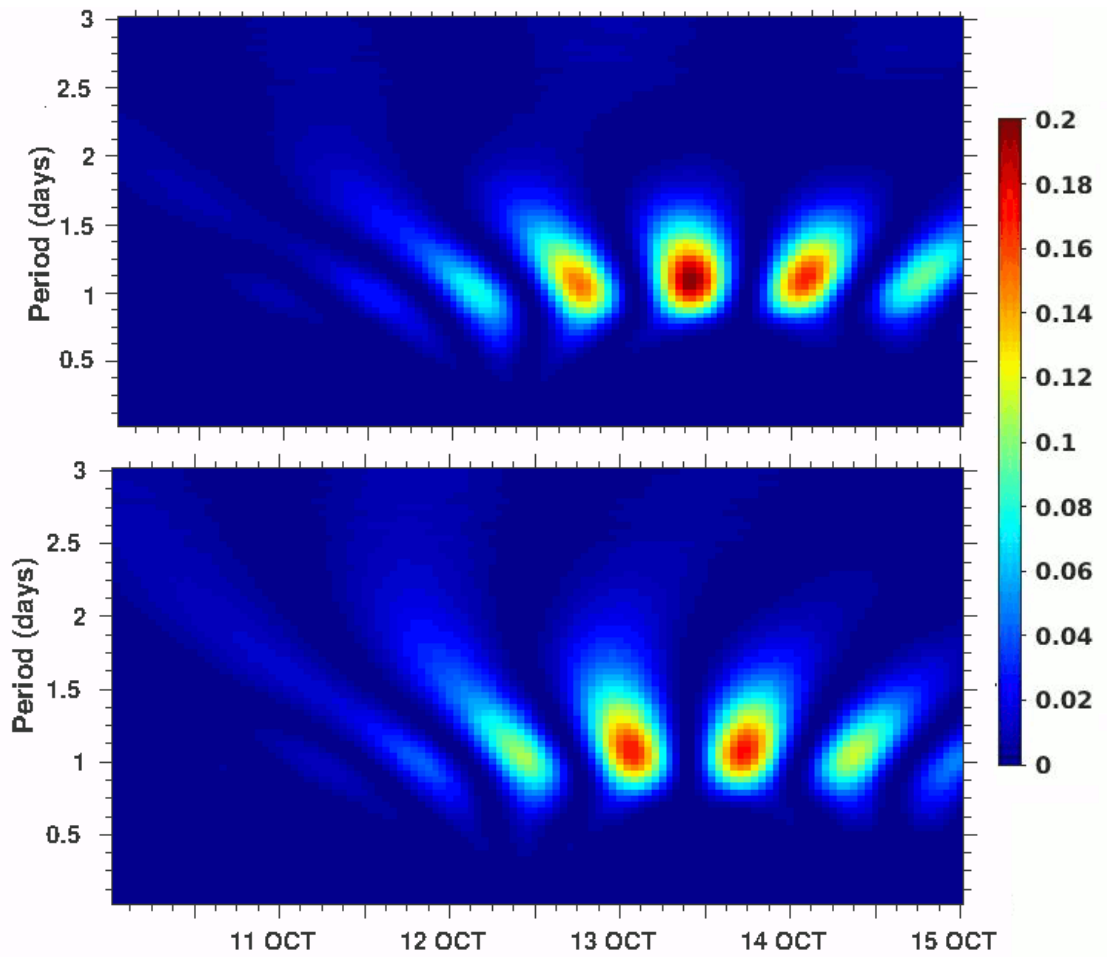


687

688 **Figure 8: Daily averaged baroclinic kinetic energy (m²s⁻²) profile at the on-track (left) and off-track**
 689 **(right) locations as marked with stars in Figure 2.**

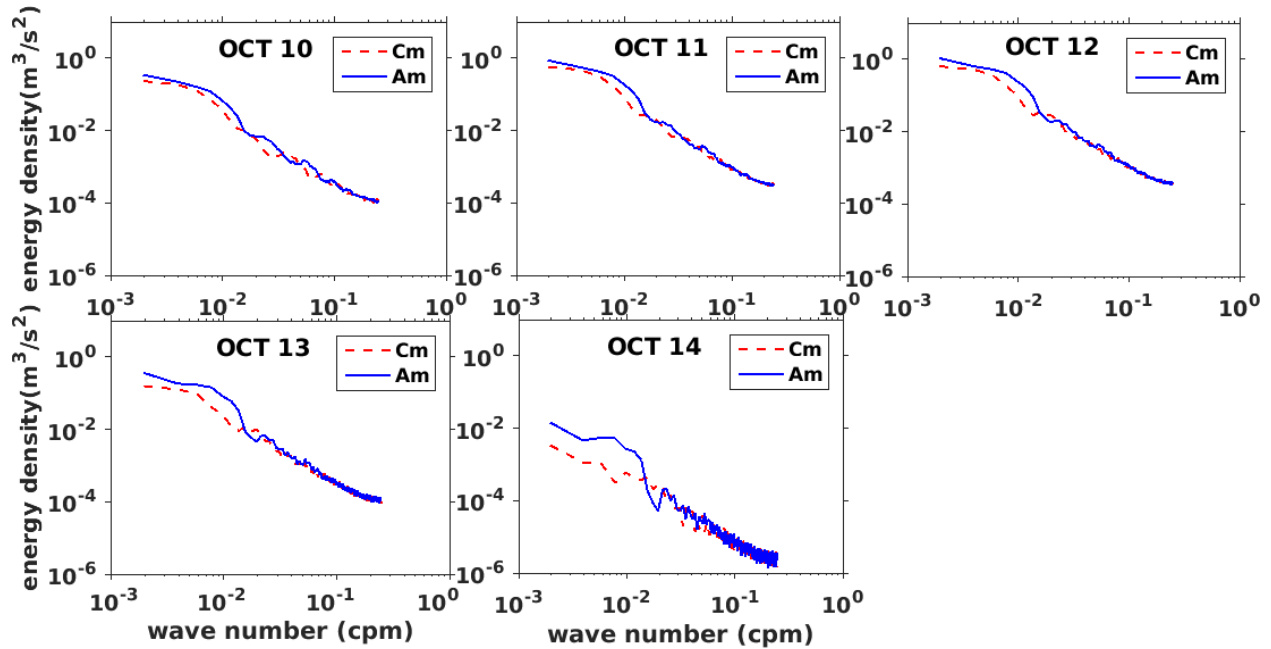
690

691



692
 693 **Figure 9:- The scalogram in percentage at 14 m depth by continuous wavelet transform (CWT)**
 694 **method. Wavelet scalogram shown for the zonal baroclinic current (upper panel) and for the**
 695 **meridional baroclinic current (lower panel).**

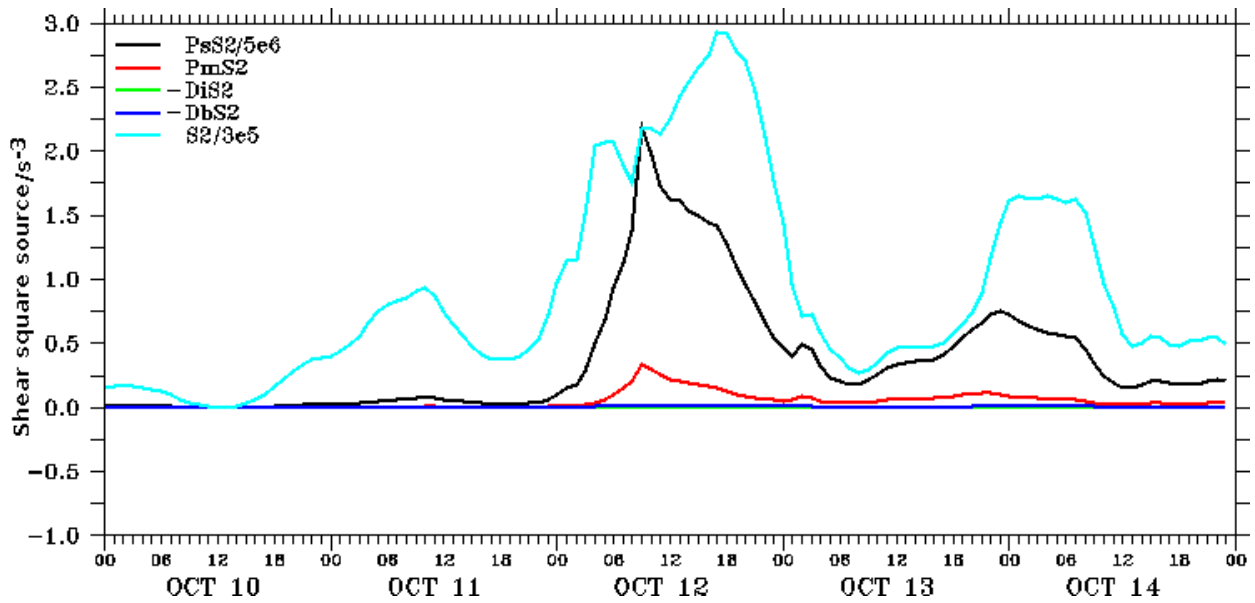
696
 697
 698
 699
 700
 701
 702



703

704 **Figure 10:-** The daily averaged vertical wave-number rotary spectra of near inertial oscillations.
 705 The anticyclonic and cyclonic spectra are represented in blue and dotted red lines respectively.

706

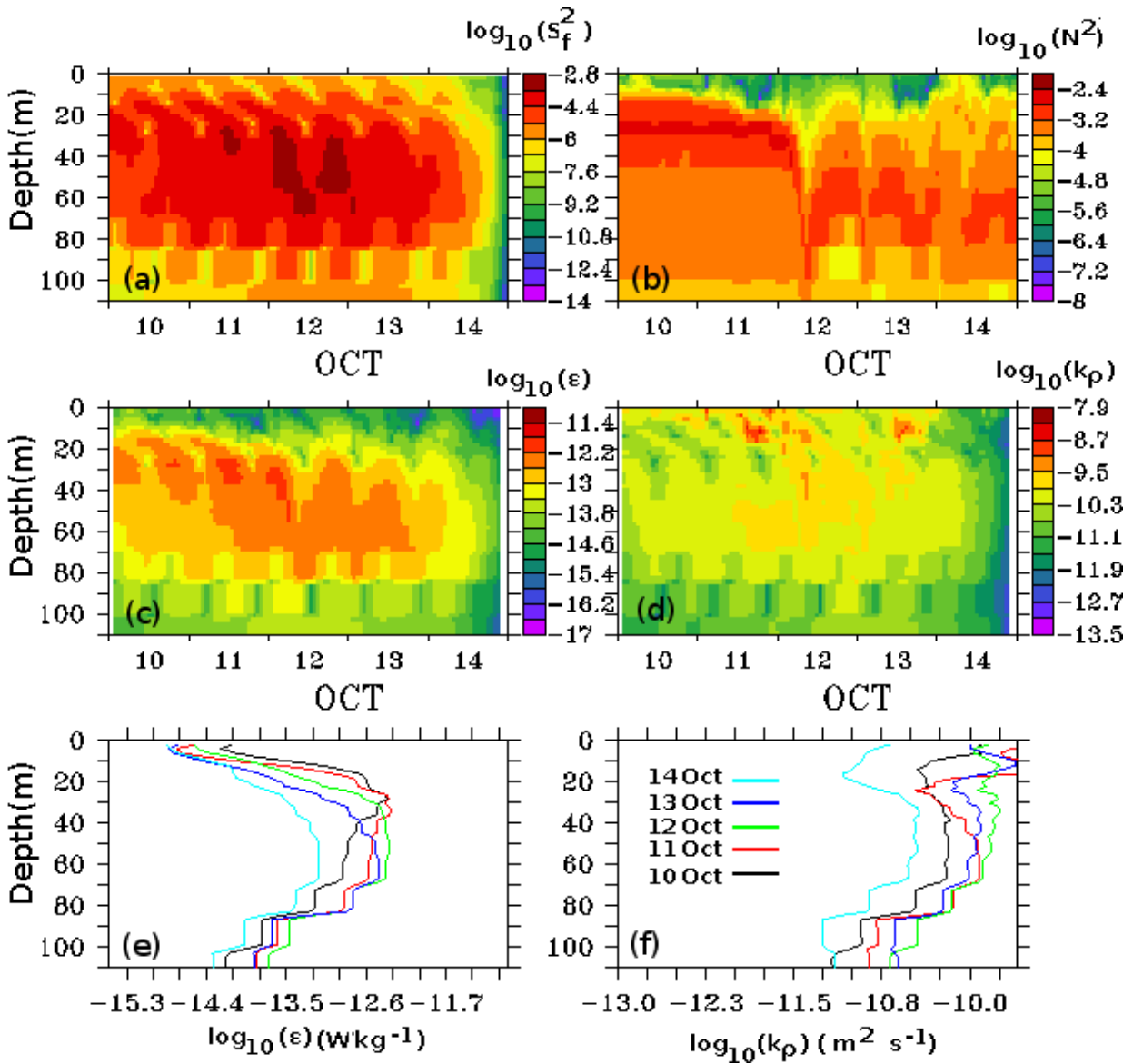


707

708 **Figure 11:-** The model simulated bulk properties at the selected point location. The vertical shear
 709 square axis is multiplied with a factor of 10^{-6} . The magnitude of bulk shear squared S^2 (cyan color),
 710 surface wind stress $P_s S^2$ (black color), barotropic effect $P_m S^2$ (red color), bottom stress $-D_b S^2$ (blue
 711 color), interfacial friction $-D_i S^2$ (green color)

712

713



714

715 **Figure 12:- Profiles of (a) velocity shear $\log_{10}(S^2)$, (b) buoyancy frequency $\log_{10}(N^2)$, (c) turbulent**
 716 **kinetic energy dissipation rate $\log_{10}(\epsilon)$, (d) turbulent eddy diffusivity $\log_{10}(K\rho)$, (e) and (f) are daily**
 717 **averaged turbulent kinetic energy dissipation rate and turbulent eddy diffusivity respectively**

718